J. Fluid Mech. (2002), *vol.* 454, *pp.* 47–69.
DOI: 10.1017/S0022112001007066 Printed in the United Kingdom

The onset of chaos in vortex sheet flow

By ROBERT KRASNY[1] AND MONIKA NITSCHE[2]

[1]University of Michigan, Ann Arbor, MI 48109-1109, USA

[2]University of New Mexico, Albuquerque, NM 87131-1141, USA

(Received 19 June 2000 and in revised form 7 September 2001)

Regularized point-vortex simulations are presented for vortex sheet motion in planar and axisymmetric flow. The sheet forms a vortex pair in the planar case and a vortex ring in the axisymmetric case. Initially the sheet rolls up into a smooth spiral, but irregular small-scale features develop later in time: gaps and folds appear in the spiral core and a thin wake is shed behind the vortex ring. These features are due to the onset of chaos in the vortex sheet flow. Numerical evidence and qualitative theoretical arguments are presented to support this conclusion. Past the initial transient the flow enters a quasi-steady state in which the vortex core undergoes a small-amplitude oscillation about a steady mean. The oscillation is a time-dependent variation in the elliptic deformation of the core vorticity contours; it is nearly time-periodic, but over long times it exhibits period-doubling and transitions between rotation and nutation. A spectral analysis is performed to determine the fundamental oscillation frequency and this is used to construct a Poincaré section of the vortex sheet flow. The resulting section displays the generic features of a chaotic Hamiltonian system, resonance bands and a heteroclinic tangle, and these features are well-correlated with the irregular features in the shape of the vortex sheet. The Poincaré section also has KAM curves bounding regions of integrable dynamics in which the sheet rolls up smoothly. The chaos seen here is induced by a self-sustained oscillation in the vortex core rather than external forcing. Several well-known vortex models are cited to justify and interpret the results.

1. Introduction

Vortex sheets are commonly used in fluid dynamics to represent thin shear layers in slightly viscous flow (Batchelor 1967; Saffman 1992). Here we present simulations of vortex sheet motion in planar and axisymmetric flow using a regularized point-vortex method. The initial condition corresponds to potential flow past either a flat plate or a circular disk, and the sheet rolls up to form a vortex pair in the planar case and a vortex ring in the axisymmetric case. The vortex pair is a model for the trailing wake behind an aircraft (Spalart 1998) and the vortex ring describes the starting flow discharged from a circular tube (Shariff & Leonard 1992; Lim & Nickels 1995). The present work is concerned with the long-time dynamics of the pair/ring.

Vortex sheet simulations encounter a number of difficulties due to Kelvin–Helmoltz instability and singularity formation (Birkhoff 1961; Moore 1979; Krasny 1986). To overcome these difficulties, we represent the sheet as a set of regularized point vortices. This approach was originally developed for vortex sheet motion in planar flow (Chorin & Bernard 1973; Anderson 1985; Krasny 1987) and was later extended to the case of axisymmetric flow (Dahm, Frieler & Tryggvason 1992; Caflisch, Li & Shelley 1993).

The regularization does not have a direct physical interpretation, but this approach gave good agreement with experiment in a simulation of axisymmetric vortex ring formation at the edge of a circular tube (Nitsche & Krasny 1994). The same type of regularization has been applied to fully three-dimensional vortex sheet motion, but this is beyond the scope of the present work; for recent developments see Brady, Leonard & Pullin (1998), Pozrikidis (2000), Lindsay & Krasny (2001), and Sakajo (2001).

As we shall see, in both the planar and axisymmetric cases the vortex sheet initially rolls up into a smooth spiral, but irregular small-scale features develop later in time: gaps and folds appear in the spiral core and a wake is shed behind the vortex ring. These features are unexpected. Similarity theory predicts a smooth regular spiral (Pullin 1978) and previous simulations ending at early times were consistent with this (Krasny 1987). We attribute the irregular features occurring here at late times to the onset of chaos in the vortex sheet flow. Numerical evidence and qualitative theoretical arguments will be presented to support this conclusion.

We find that past the initial transient, the vortex sheet flow enters a quasi-steady state in which the vortex core undergoes a small-amplitude oscillation about a steady mean. The oscillation is characterized as a time-dependent variation in the elliptic deformation of the core vorticity contours, resembling the time-periodic motion of an elliptic vortex patch in a strain field (Moore & Saffman 1971; Kida 1981; Neu 1984). However the oscillation seen here is not exactly time-periodic; over long times it exhibits period-doubling and transitions between rotation and nutation. A spectral analysis is performed to determine the fundamental oscillation frequency and this is used to construct a Poincaré section of the vortex sheet flow. The resulting section displays the generic features of a chaotic Hamiltonian system, resonance bands and a heteroclinic tangle, and these features are well-correlated with the irregular features in the shape of the vortex sheet. The Poincaré section also has KAM curves bounding regions of integrable dynamics in which the sheet rolls up smoothly. We conclude that the chaos seen here is induced by a self-sustained oscillation in the vortex core rather than external forcing.

The connection between Hamiltonian chaos and incompressible fluid flow has received increasing attention in recent years (Aref 1983; Ottino 1989). Many of these investigations focus on vortex-dominated flows and here we briefly describe some of the work in this area in order to set the context for the present findings (see Newton 2001 for further discussion and references). Aref (1984) studied chaotic advection of passive particles in a model of a stirred tank where the flow was generated by two point vortices that alternately turn on and off. Polvani & Wisdom (1990) studied chaotic advection in the flow induced by an elliptic vortex patch in a steady strain field, and Dhanak & Marshall (1993) showed that adding a time-dependent perturbation to the strain field can destabilize the regular patch dynamics. Shariff, Leonard & Ferziger (1989) simulated leap-frogging of vortex rings and showed that the unstable manifold in the simulation resembles the wake seen in experiments; the shape of the manifold indicated that a heteroclinic tangle is present in the dynamics. Lopez & Perry (1992) reached a similar conclusion for the wake behind the breakdown region in a simulation of swirl flow in a cylindrical tube; their simulation also predicted a resonance band in the breakdown region and this was later confirmed experimentally by Stevens, Lopez & Cantwell (1999). Miller *et al.* (1997) simulated an oceanic jet and studied transport across the jet boundaries due to a heteroclinic tangle.

Much of the work in this area is computational, but in certain cases where an autonomous system is subject to time-periodic forcing, Melnikov's technique can be

applied to prove analytically that chaos occurs. Using this approach, Bertozzi (1988) showed that chaos occurs in the dynamics of an elliptic vortex patch subject to time-periodic straining, while Ide & Wiggins (1995) gave phase diagrams describing the chaotic transitions in the patch dynamics. Rom-Kedar, Leonard & Wiggins (1990) applied Melnikov's technique to study chaotic advection and transport in the flow induced by an oscillating vortex pair. These two models, the oscillating vortex pair and the strained elliptic vortex patch, are especially relevant for the present work and we will discuss them later in more detail. For now we emphasize that they can exhibit two different types of behaviour. In the case of the oscillating vortex pair and the elliptic vortex patch with steady strain, the vorticity distribution has integrable dynamics (although there is chaotic advection of passive particles in the induced velocity field). However in the case of the elliptic vortex patch with time-periodic strain, the vorticity distribution itself has chaotic dynamics. As will be seen, there is evidence for both types of behaviour in the vortex sheet flow.

The paper is organized as follows. The problem is formulated in § 2. Simulations are presented in § 3 showing the development of irregular features in the shape of the vortex sheet. Some well-known properties of chaotic Hamiltonian systems are reviewed in § 4. The evidence concerning chaos in the vortex sheet flow is given next including a description of the quasi-steady state in § 5, a spectral analysis of the vortex core oscillation in § 6, and a numerically generated Poincaré section in § 7. In § 8 we discuss several questions that arise, and a summary and concluding remarks are given in § 9. A preliminary account of this work was presented by Nitsche (1998).

2. Problem formulation

This section presents the initial condition, evolution equation, and numerical method. Further details can be found in Krasny (1987) and Nitsche & Krasny (1994).

2.1. *Initial condition*

The problem is formulated in terms of Cartesian coordinates (x, y, z) in the planar case and cylindrical coordinates (x, y, θ) in the axisymmetric case; note that x is a linear axial coordinate in both cases, and y is a linear coordinate in the planar case and a radial coordinate in the axisymmetric case. The initial condition is the potential flow past either a flat plate or a circular disk that approaches a uniform stream at infinity. Figure 1 shows the streamlines of the flow, with the sheet appearing as a vertical line segment. The problem is completely specified by two variables: Y, the plate half-span or disk radius, and U, the far-field velocity amplitude. In terms of these variables, the maximum circulation on the sheet is $\Gamma_0 = cUY$, where $c_{2d} = 2$, $c_{3d} = 4/\pi$ (Lamb 1932; throughout this work subscripts $2d$ and $3d$ denote the planar and axisymmetric cases, respectively). The results below are given in nondimensional form with distance scaled by Y and time scaled by Y^2/Γ_0. With this scaling, $\Gamma_0 = 1$ in both cases.

The vortex sheet is defined by a curve $(x(\alpha, t), y(\alpha, t))$ in a cross-section of the fluid domain, where α is a material parameter along the curve and t is time. The sheet is assumed to be symmetric about the x-axis in the planar case and this condition is satisfied by definition in the axisymmetric case. The initial parametrization of the sheet is $x(\alpha, 0) = 0$, $y(\alpha, 0) = \cos\alpha$ for $0 \leqslant \alpha \leqslant \frac{1}{2}\pi$, and the circulation due to the potential flow is $\Gamma(\alpha) = \sin\alpha$. The circulation on the sheet satisfies $\Gamma \sim s^{1/2}$, where s is distance from the edge; the branch point singularity causes the sheet to roll up into a spiral for $t > 0$ (Pullin 1978).

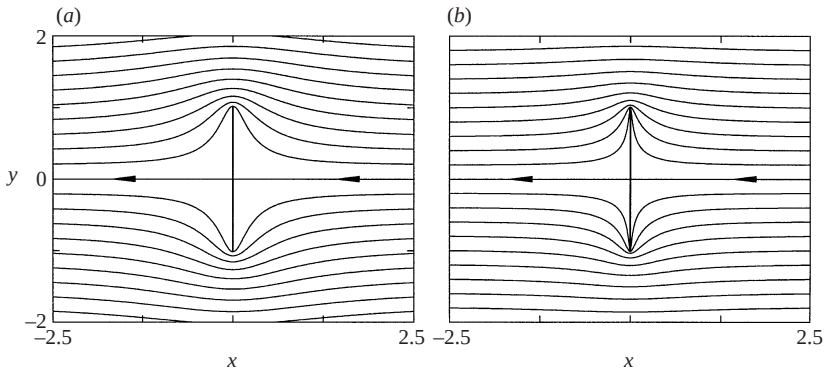

FIGURE 1. Streamlines of the initial potential flow: (*a*) planar flow past a flat plate; (*b*) axisymmetric flow past a circular disk. The vortex sheet appears as a vertical line segment.

2.2. *Evolution equation*

The vortex sheet is a superposition of basic elements, either point vortices or circular vortex lines. In planar flow, the stream function at (x, y) due to a pair of counter-rotating point vortices located at $(\tilde{x}, \pm\tilde{y})$ is

$$\psi_{2d}(x, y; \tilde{x}, \tilde{y}) = -\frac{1}{4\pi} \log \frac{(x-\tilde{x})^2 + (y-\tilde{y})^2 + \delta^2}{(x-\tilde{x})^2 + (y+\tilde{y})^2 + \delta^2}, \tag{2.1}$$

and in axisymmetric flow, the stream function at (x, y) due to a circular vortex line located at $(\tilde{x}, \tilde{y})$ is

$$\psi_{3d}(x, y; \tilde{x}, \tilde{y}) = \frac{1}{4\pi} \int_0^{2\pi} \frac{y\tilde{y}\cos\theta}{((x-\tilde{x})^2 + y^2 + \tilde{y}^2 - 2y\tilde{y}\cos\theta + \delta^2)^{1/2}} \mathrm{d}\theta. \tag{2.2}$$

In these expressions, the variable δ plays the role of a smoothing parameter and the exact values of ψ_{2d}, ψ_{3d} are recovered by setting δ to zero. The stream function associated with the vortex sheet is obtained by integrating along the curve,

$$\psi_{2d,3d}(x, y, t) = \int_0^{\pi/2} \psi_{2d,3d}(x, y; x(\alpha, t), y(\alpha, t)) \mathrm{d}\Gamma(\alpha). \tag{2.3}$$

The velocity induced by the sheet is obtained by differentiating the stream function,

$$u = \frac{\partial \psi_{2d}}{\partial y}, \quad v = -\frac{\partial \psi_{2d}}{\partial x}, \qquad u = \frac{1}{y}\frac{\partial \psi_{3d}}{\partial y}, \quad v = -\frac{1}{y}\frac{\partial \psi_{3d}}{\partial y}, \tag{2.4}$$

where the arguments (x, y, t) have been dropped for clarity. Finally, the sheet evolves by self-induction,

$$\frac{\partial x}{\partial t} = u(x, y), \quad \frac{\partial y}{\partial t} = v(x, y), \tag{2.5}$$

where $x = x(\alpha, t)$, $y = y(\alpha, t)$ and the velocity components u, v are integrals obtained from (2.4).

2.3. *Numerical method*

The sheet is represented by regularized point vortices, $(x_j(t),\ y_j(t))$, $j = 1, \ldots, N$, corresponding to a discretization in the parameter α. The points satisfy a system of ordinary differential equations in time obtained by applying the trapezoid rule to the

velocity integrals on the right of (2.5). Time-stepping is performed by the fourth-order Runge–Kutta method. The initial discretization is uniform in α and additional points are inserted to maintain resolution as the sheet rolls up. The point insertion scheme relies on two user-specified parameters, ϵ and N_c. Two conditions are enforced: (i) the distance between any two consecutive points on the sheet is less than ϵ, and (ii) the angular displacement with respect to the spiral centre between any two consecutive points is less than $2\pi/N_c$. The location of an inserted point is determined by local cubic polynomial interpolation with respect to the material parameter α.

In this work the value $\delta = 0.2$ is chosen for the smoothing parameter; this is meant as a representative value. The remaining numerical parameters are chosen to obtain an accurate solution of the vortex sheet evolution equation (2.5) for the given value of δ. In the present simulations, the timestep is $\Delta t = 0.025$, and the point insertion parameters are $\epsilon = 0.04$, $N_c = 25$ in the planar case and $\epsilon = 0.10$, $N_c = 22$ in the axisymmetric case. The initial number of points is $N = 400$. The planar simulation was terminated at $t = 120$ with $N = 6159$ points and the axisymmetric simulation was terminated at $t = 60$ with $N = 3776$ points. Mesh-refinement tests were performed to ensure that the computed solution is well-resolved. The simulations were performed on a Sparc 10 workstation, requiring approximately 14 h in the planar case and 33 h in the axisymmetric case.

3. Irregular features in the shape of the vortex sheet

Figure 2 shows the numerical solution up to time $t = 120$ in the planar case and $t = 60$ in the axisymmetric case. The edge of the sheet rolls up into a spiral, forming a planar vortex pair and an axisymmetric vortex ring, respectively. The sheet gradually fills an elliptic region, or oval, which translates in the x-direction. The major axis of the oval is normal to the translation direction, and the oval has smaller area and larger aspect ratio in the axisymmetric case than in the planar case. The vortex sheet spiral has a smooth regular shape at early times, but irregular small-scale features develop later on. A long thin wake is shed behind the vortex ring and there is a disturbance in the vortex core in both cases.

Figure 3 shows the onset of the irregular features at intermediate times. In the planar case (figure 3*a*), gaps form in the spiral core and the regular spacing between the turns is upset. The disturbance is confined to a thin annular band, and the sheet rolls up smoothly away from the band. In the axisymmetric case (figure 3*b*), the roll-up is smooth everywhere except near the back of the ring where folds appear in the outer turn. The folds become sharper in time and are stretched in the x-direction. New folds continually appear and the process repeats.

Figure 4 shows a close-up of the vortex sheet at the final simulation time. In the planar case (figure 4*a*), gaps and now also folds appear, though still confined to a thin annular band. In the axisymmetric case (figure 4*b*), there is now a disturbance in the core, though more dispersed than in the planar case. Away from the core, the outer turns of the sheet remain smooth in the planar case, but in the axisymmetric case they are folded and stretched near the back of the ring. Some parts of the sheet trail behind the ring and form a wake, while other parts are advected forward inside the ring.

The irregular small-scale features in the shape of the vortex sheet are unexpected. Previous simulations in the planar case terminated at earlier times when the roll-up is still smooth (Krasny 1987). It was known that a semi-infinite vortex sheet with a branch point singularity at the edge rolls up in a self-similar manner (Pullin 1978) and

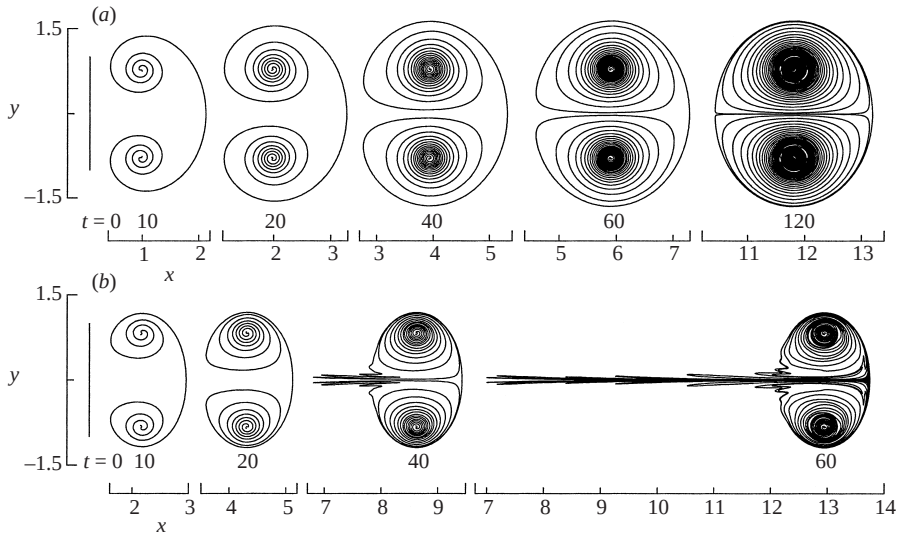

FIGURE 2. Computed vortex sheet at the indicated times: (*a*) planar vortex pair, $0 \leqslant t \leqslant 120$; (*b*) axisymmetric vortex ring, $0 \leqslant t \leqslant 60$.

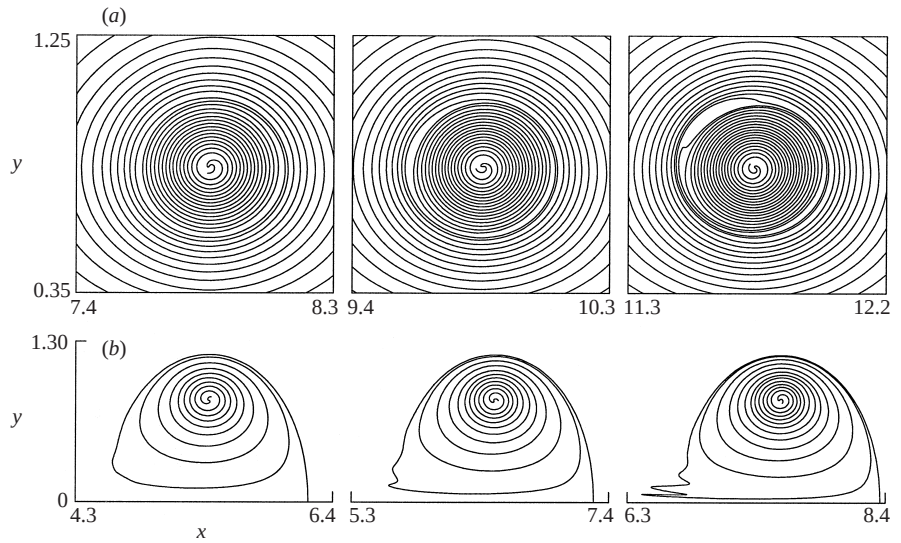

FIGURE 3. Onset of irregular small-scale features in the shape of the vortex sheet at intermediate times: (*a*) planar, $t = 80, 90, 100$; (*b*) axisymmetric, $t = 25, 30, 35$ (left to right).

the earlier simulations had indicated that the core of the planar vortex pair follows the self-similar scaling laws. Based on those results, it was assumed that the sheet rolls up smoothly for all time, gradually filling in more of the oval. From that point of view it is natural to suspect that the irregular features seen here are numerical artifacts, but we performed extensive tests and found that the present results are converged with respect to mesh refinement in the spatial and temporal discretization. Similar results are obtained for different values of the smoothing parameter δ, the main difference being that as δ is reduced, the sheet rolls up faster and more tightly, and the irregular features occur sooner. We conclude that the irregular features are genuine, at least in

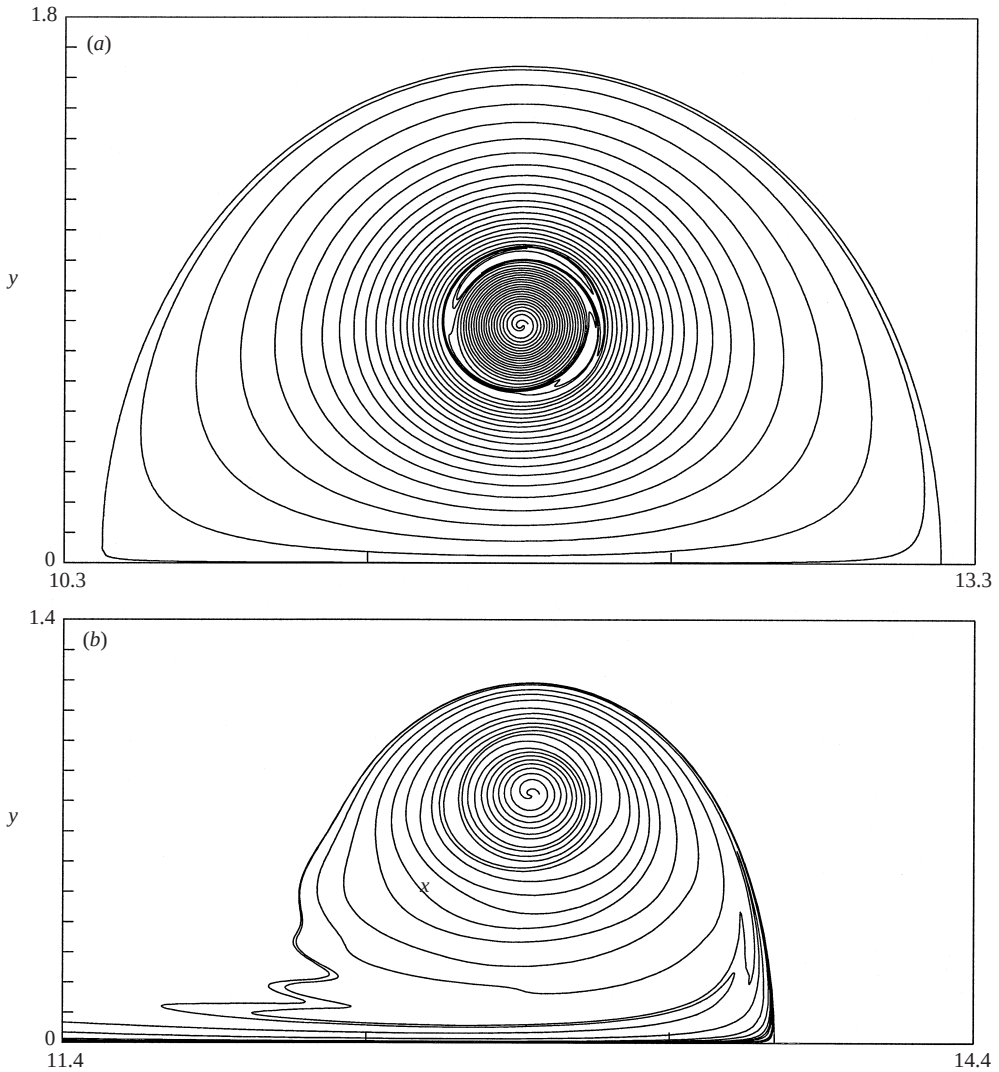

FIGURE 4. Close-up of the vortex sheet at the final simulation time: (*a*) planar, $t = 120$; (*b*) axisymmetric, $t = 60$.

so far as the present regularized vortex sheet model is concerned; the remainder of this paper is devoted to showing that they are a manifestation of chaos.

4. Chaotic Hamiltonian systems

In this section we review some well-known properties of chaotic Hamiltonian systems (Guckenheimer & Holmes 1983; Wiggins 1992). This provides the background needed for our subsequent discussion of the vortex sheet flow. We start by noting that the motion of material points in planar incompressible fluid flow is governed by a Hamiltonian system,

$$\frac{\mathrm{d}x}{\mathrm{d}t} = \frac{\partial \psi}{\partial y}, \quad \frac{\mathrm{d}y}{\mathrm{d}t} = -\frac{\partial \psi}{\partial x}, \tag{4.1}$$

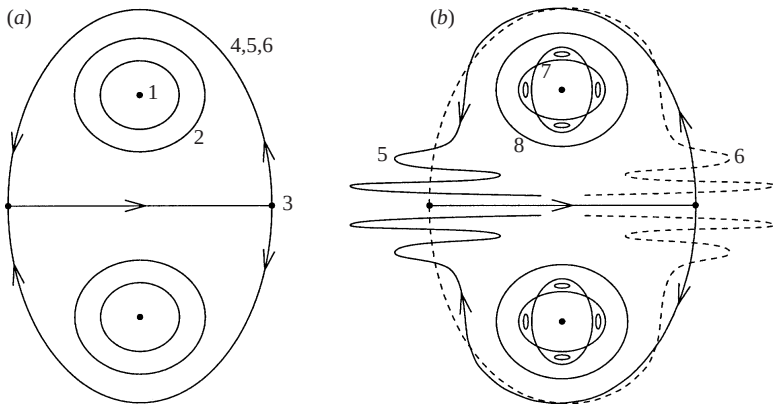

FIGURE 5. Schematic view of the dynamics in the oscillating vortex pair model of Rom-Kedar *et al.* (1990): (*a*) streamlines of unperturbed flow, $\epsilon = 0$; (*b*) Poincaré section of perturbed flow, $\epsilon > 0$. 1: Elliptic point; 2: periodic orbit; 3: hyperbolic point; 4: heteroclinic orbit; 5: unstable manifold of front hyperbolic point (solid); 6: stable manifold of back hyperbolic point (dashed). 7: resonance band; 8: KAM curve or cantorus. Arrows indicate the direction of increasing time.

where the stream function $\psi(x, y, t)$ plays the role of the Hamiltonian. A similar result holds for axisymmetric flow. In this context, the phase space of the Hamiltonian system is the physical x, y-space of the fluid flow and using this correspondence, the theory of dynamical systems can be applied to derive properties of the fluid flow.

One example that is especially relevant for the present work is the oscillating vortex pair (OVP) model of Rom-Kedar *et al.* (1990). They considered a stream function of the form

$$\psi(x, y, t) = \psi_0(x, y) + \epsilon\psi_1(x, y, t), \tag{4.2}$$

where $\psi_0(x, y)$ is the steady flow defined by a pair of counter-rotating point vortices, $\psi_1(x, y, t)$ is a time-periodic perturbation strain field, and ϵ is the perturbation amplitude. The system is integrable for $\epsilon = 0$ and chaotic for $\epsilon > 0$. Figure 5 gives a schematic view of the dynamics in the OVP model. For $\epsilon = 0$, the point vortices translate with constant velocity and figure 5(*a*) depicts the streamlines of the flow in a reference frame moving with the vortices. Several different types of orbits occur. The point vortices are elliptic points surrounded by periodic orbits. Each periodic orbit has an associated rotation number, defined as the ratio between the period of the orbit and the period of the forcing term ψ_1. The periodic orbits are contained in an oval. There are two hyperbolic points, one in front of the oval and one in back. The unstable manifold of the front hyperbolic point coincides with the stable manifold of the back hyperbolic point, and the two manifolds form a heteroclinic orbit connecting the hyperbolic points. These are all of the bounded orbits in the unperturbed flow; there are also unbounded orbits outside the oval (not shown).

Periodic forcing has a dramatic effect on the dynamics. This is not evident from instantaneous streamlines of the perturbed flow; with small forcing amplitude, the streamlines of the perturbed flow have the same pattern as for the unperturbed flow. To understand the dynamics of the perturbed flow, one instead samples the orbits at the forcing frequency to obtain a Poincaré section, shown schematically in figure 5(*b*). In this case, the stable and unstable manifolds intersect transversely. The unstable manifold of the front hyperbolic point is folded and stretched as $t \to +\infty$, and the stable manifold of the back hyperbolic point behaves similarly as $t \to -\infty$. The

intersecting manifolds form a heteroclinic tangle and it follows that the system has chaotic dynamics. Moreover, a periodic orbit of the unperturbed flow having rational rotation number breaks up into a resonance band (also called an island chain or stochastic layer). A resonance band has a sequence of elliptic and hyperbolic periodic points, and these in turn give rise to secondary resonance bands and heteroclinic tangles. On the other hand, a periodic orbit of the unperturbed flow having irrational rotation number does not break up into a resonance band, but instead forms either a KAM curve or a cantorus.

This concludes our qualitative description of chaotic dynamics in the OVP model. Rom-Kedar *et al.* (1990) applied Melnikov's technique to prove that chaos occurs and made a detailed study of the resulting particle transport. We note that the OVP model has a similar structure to the vortex sheet flow; in particular, the counter-rotating point-vortices in the OVP model are analogous to the vortex cores in the pair/ring. More significantly, the chaotic features in the Poincaré section of the perturbed OVP model are reminiscent of the irregular small-scale features in the shape of the vortex sheet: the wake behind the vortex ring resembles a heteroclinic tangle and the gaps in the spiral core suggest a resonance band. In fact, this is more than just a coincidence and as we shall see, the vortex sheet flow has chaotic dynamics in much the same sense as the OVP model. The next three sections present evidence to support this conclusion. The first observation is that past the initial transient the vortex sheet flow enters a quasi-steady state. In this regime the vortex core undergoes a small-amplitude oscillation which is close to time-periodic. Using the oscillation frequency, we construct a Poincaré section of the vortex sheet flow and observe that it has the generic features of a chaotic Hamiltonian system.

5. Quasi-steady state

Figure 6 displays the vortex sheet, streamlines, and vorticity contours at time $t = 40$, a representative time past the initial transient. The streamlines of the vortex sheet flow (figure 6*b*,*e*) have the same pattern as the unperturbed OVP flow (figure 5*a*). The closed streamlines form an oval and the vortex sheet lies inside the oval, except for the wake behind the vortex ring in the axisymmetric case. To construct vorticity contour plots, the vorticity $\omega(x, y, t)$ was evaluated on a regular mesh by taking the curl of the velocity (2.4). The smoothing parameter δ ensures that the computed vorticity is continuous. The vorticity is positive for $y > 0$ and negative for $y < 0$. The highest vorticity contour appearing in figure 6 is closest to the centre of the core and has amplitude $|\omega| = 4$. Consecutive contours decrease by a factor of $1/2$, and since the plotted contours are almost equally spaced, it follows that the vorticity decays exponentially with distance from the centre of the core. In the vorticity contour plots, the edge of the streamline oval is shown as a dashed line. Note that the vortex core is closer to the edge of the oval in the axisymmetric case than in the planar case.

Figure 7 plots the profiles of induced axial velocity u and vorticity ω along a vertical line $0 \leqslant y \leqslant 2$ through the centre of the core at time $t = 40$. The profiles are similar in the planar and axisymmetric cases. The main difference is in the velocity: for a given location y, the velocity induced by the axisymmetric ring (figure 7*b*) is greater than the velocity induced by the planar pair (figure 7*a*). The vorticity profiles have a smooth peaked shape consistent with the contour plots above. A long dashed line in figure 7 indicates the centre of the core as determined by the point of maximum vorticity; this occurs at approximately $y = 0.8$ in both cases, showing that the pair and the ring have the same large-scale radius. A short dashed line indicates the edge

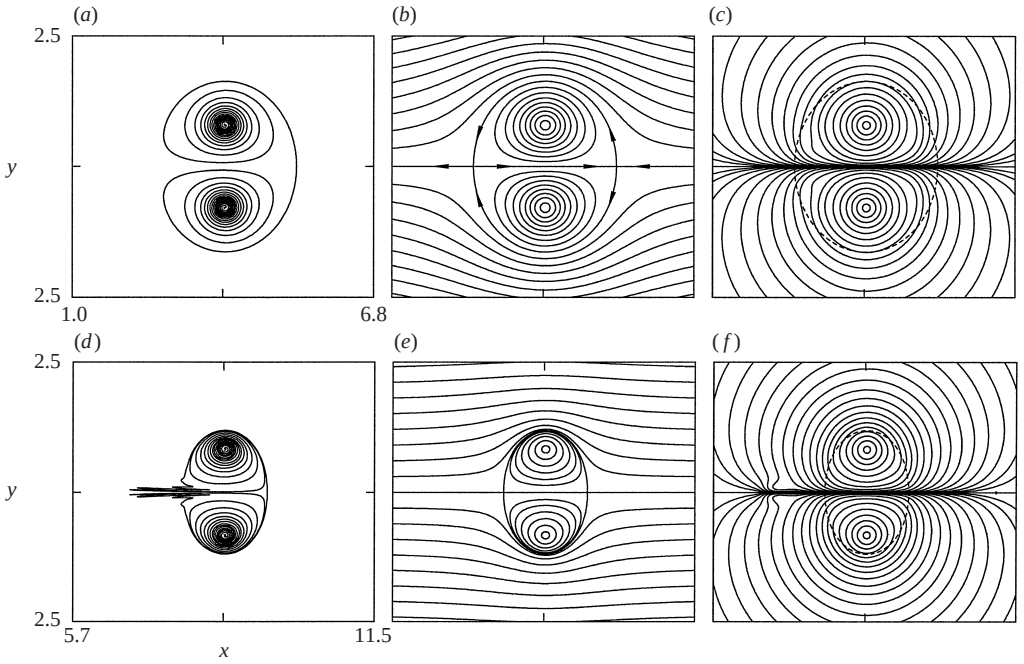

FIGURE 6. Computed solution at time $t = 40$: (a, d) vortex sheet; (b, e) streamlines; (c, f) vorticity contours; planar (top); axisymmetric (bottom). The vorticity is positive for $y > 0$ and negative for $y < 0$. The highest vorticity contour is closest to the centre of the core and has amplitude $|\omega| = 4$. Consecutive contours decrease by a factor of $1/2$.

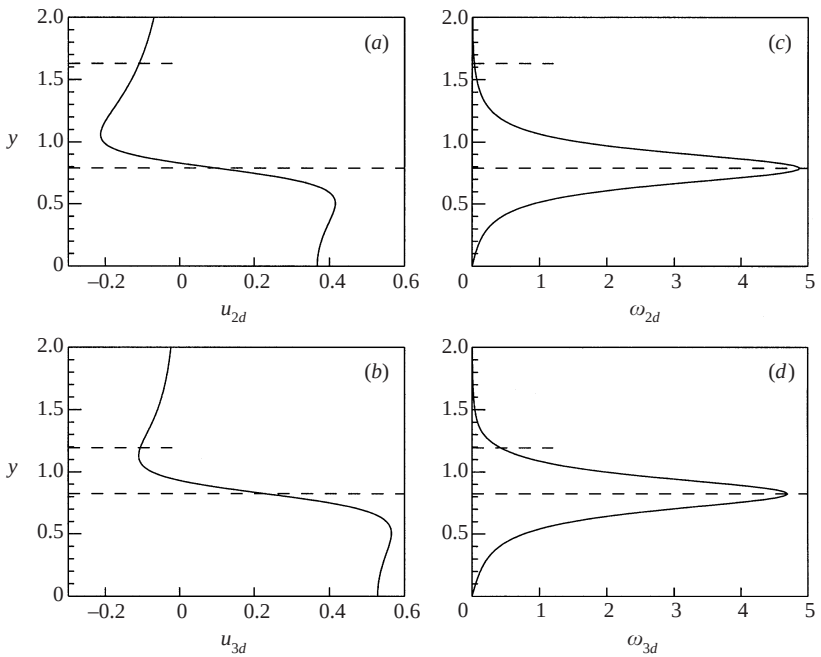

FIGURE 7. Profiles along a vertical line through the centre of the core at time $t = 40$. (a, b) u_{2d}, u_{3d}: induced axial velocity; (c, d) ω_{2d}, ω_{3d}: vorticity. A long dashed line indicates the centre of the core and a short dashed line indicates the edge of the streamline oval.

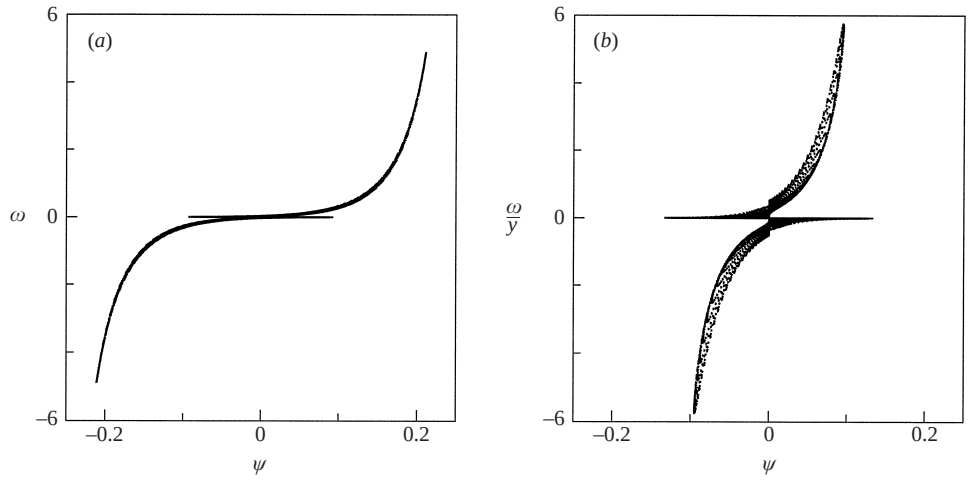

FIGURE 8. Scatterplot of the stream function and vorticity at time $t = 40$: (a) planar (ψ, ω); (b) axisymmetric $(\psi, \omega/y)$.

of the streamline oval; this occurs at $y = 1.6$ in the planar case and $y = 1.2$ in the axisymmetric case, showing again that the vortex core is closer to the edge of the oval in the axisymmetric case.

Figures 6 and 7 are concerned with instantaneous properties of the flow at time $t = 40$, but the results are effectively indistinguishable at any other time past the initial transient. This indicates that the vortex sheet flow is close to a steady state. To check this assertion, figure 8 presents a scatterplot of the stream function and vorticity. In steady ideal flow these quantities satisfy a functional relation, $\omega = f(\psi)$ in the planar case and $\omega/y = f(\psi)$ in the axisymmetric case. The data in figure 8 show that such relations are approximately satisfied and this supports the conclusion that the vortex sheet flow is close to a steady state. Note that the data are more dispersed in figure 8(b) than in figure 8(a), suggesting that the flow is closer to a true steady state in the planar case than in the axisymmetric case. The scatterplots obtained here resemble the nonlinear profiles seen in some previous simulations (e.g. Couder & Basdevant 1986; Montgomery *et al.* 1993; Shariff, Verzicco & Orlandi 1994).

Figure 9 plots the translation velocity $\bar{u}(t)$ of the pair/ring, defined by $\bar{u} = \mathrm{d}\bar{x}/\mathrm{d}t$, where $\bar{x}_{2d} = \int x \mathrm{d}\Gamma / \int \mathrm{d}\Gamma$ and $\bar{x}_{3d} = \int xy^2 \mathrm{d}\Gamma / \int y^2 \mathrm{d}\Gamma$ (Lamb 1932). We note in passing that the stream function displayed above in figures 6 and 8 was computed in a reference frame moving with velocity $\bar{u}(t = 40)$. Figure 9(a) shows that past the initial transient, $\bar{u}(t)$ is almost constant in time; the values are approximately $\bar{u}_{2d} = 0.10$ in the planar case and $\bar{u}_{3d} = 0.22$ in the axisymmetric case. Hence the axisymmetric ring travels slightly more than twice as fast as the planar pair and this is consistent with the axial location of the sheet in figure 2. A small-amplitude oscillation is evident in the translation velocity of the axisymmetric ring (figure 9a). A close-up shows that the translation velocity of the planar pair also oscillates (figure 9c), but with smaller amplitude than for the axisymmetric ring (figure 9b). The results support the previous finding that the flow is closer to a steady state in the planar case than in the axisymmetric case.

Figures 6–9 show that past the initial transient, the vortex sheet flow enters a quasi-steady state in which the pair/ring translation velocity undergoes a small-amplitude oscillation in time. Several previous investigators have shown that oscillations can

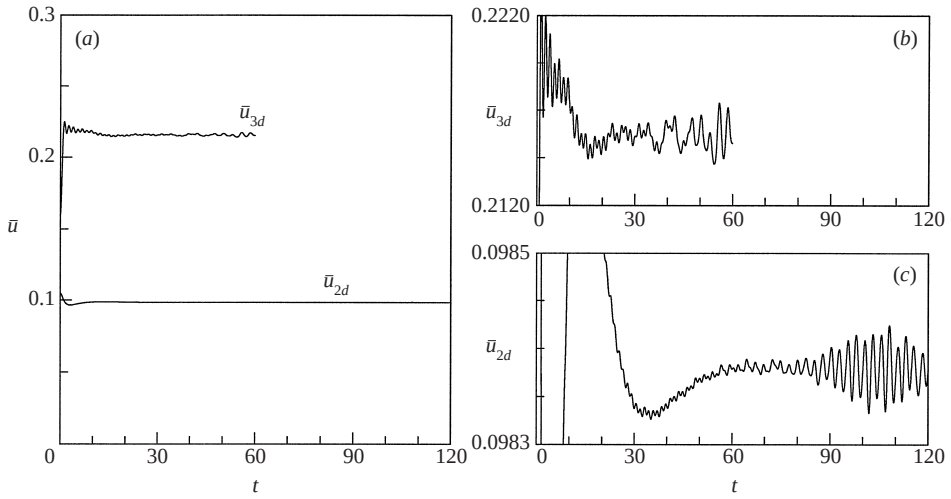

FIGURE 9. Translation velocity $\bar{u}(t)$ of the pair/ring: (a) planar ($2d$), axisymmetric ($3d$); (b) axisymmetric close-up; (c) planar close-up.

occur in the translation velocity of a vortex ring and are related to oscillations in the shape of the core. In particular, Moore (1980) showed that a vortex ring with a rotating core of elliptic cross-section has a time-periodic translation velocity, and Ye & Chu (1995) showed that a perturbed Norbury vortex ring has oscillations in the translation velocity and the shape of the core. In view of these results, the oscillation in the pair/ring translation velocity displayed in figure 9 may indicate that an oscillation is occurring in the shape of the vortex core. We examine this issue in the next section.

6. Oscillations in the vortex core

The core vorticity contours in the quasi-steady state appear circular in shape (figure 6), but there is a small departure from radial symmetry that can be measured as follows. Let $r(\theta)$ denote the radius of a contour as a function of the angle θ about the centre, and consider the Fourier series

$$r(\theta) = \sum_m \hat{r}_m \exp(\mathrm{i}m\theta). \tag{6.1}$$

The $m = 0$ mode defines the mean radius of the contour, the $m = 1$ mode shifts the centre of the contour, the $m = 2$ mode is an elliptic deformation in the shape of the contour, and $m \geqslant 3$ yields higher modes of deformation. Figure 10 plots the modal amplitudes $|\hat{r}_m|$ as a function of the wavenumber m for four vorticity contour levels ($\omega = 3.6, 2.4, 1.2, 0.6$) at time $t = 40$. In this analysis, the centre of a contour is determined using an iterative scheme that ensures $|\hat{r}_1|$ is small. Referring to figure 10, the radial mode has the largest amplitude, followed by the elliptic mode which is at least an order of magnitude smaller. Higher modes are present, but the amplitudes $|\hat{r}_m|$ decay rapidly as m increases. Note that for each wavenumber m, the corresponding modal amplitude increases as the contour level decreases; in other words, the contours become less circular moving away from the centre of the core (this can be seen in the contour plots in figure 6).

Figure 11 plots the amplitude of the elliptic mode $|\hat{r}_2|$ as a function of time for

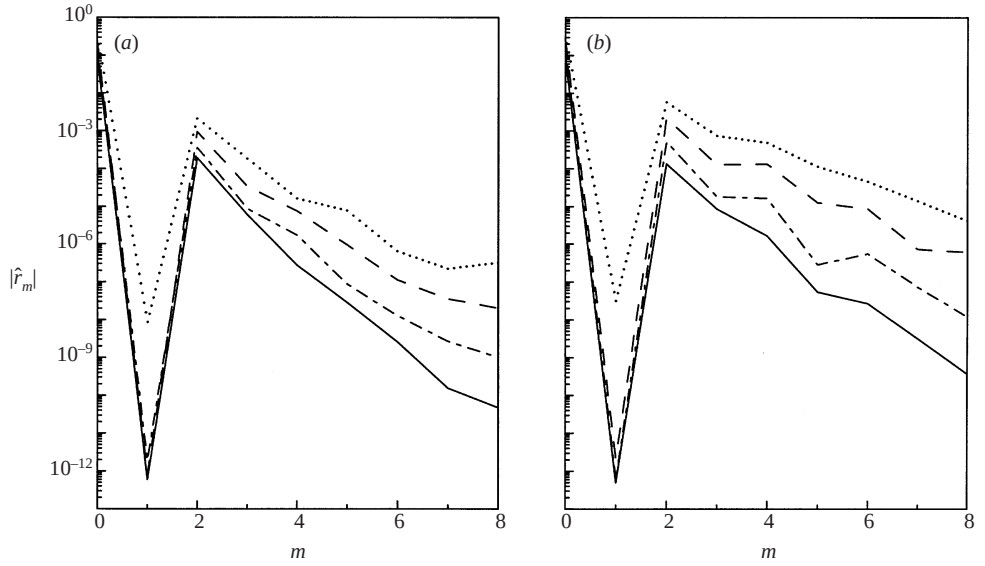

FIGURE 10. Modal amplitudes $|\hat{r}_m|$ of the core vorticity contours (6.1), plotted as a function of wavenumber m at time $t = 40$: (a) planar; (b) axisymmetric. The vorticity contour levels are $\omega = 3.6$ (——); 2.4 (– – –); 1.2 (– –); 0.6 (· · · ·).

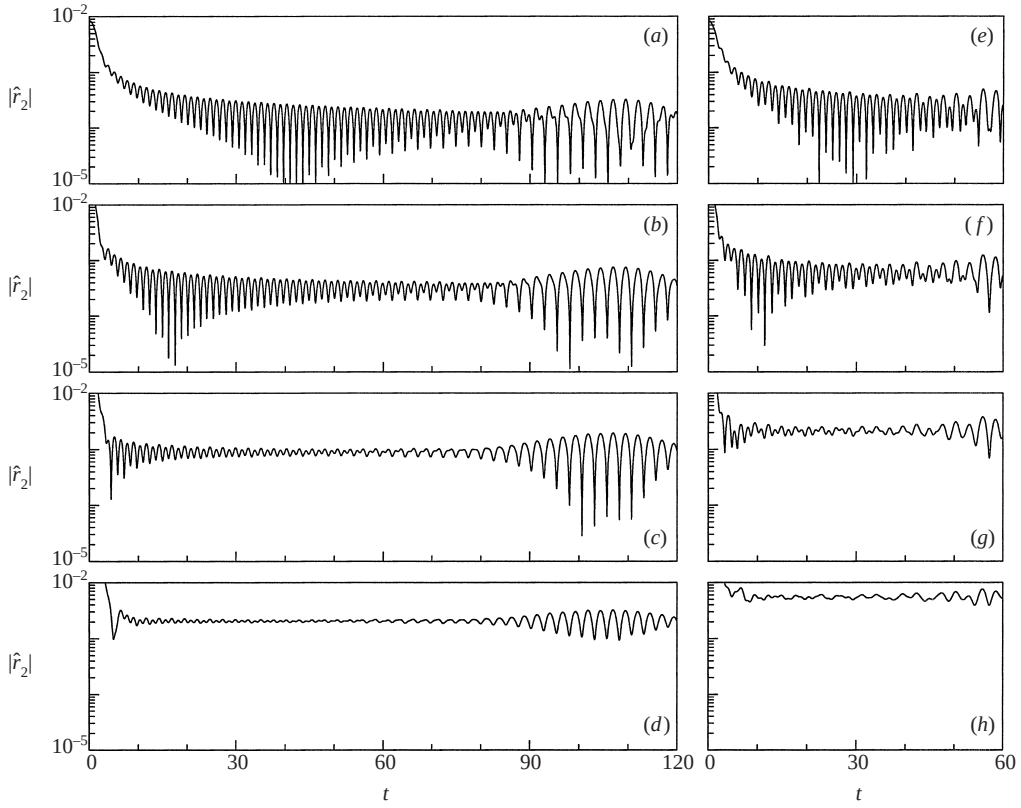

FIGURE 11. The amplitude $|\hat{r}_2|$ of the elliptic mode in the core vorticity contours, plotted as a function of time: planar (left); axisymmetric (right). The vorticity contour levels are $\omega = 3.6$ (a, e); 2.4 (b, f); 1.2 (c, g); 0.6 (d, h).

the same vorticity contour levels as in figure 10. The value of $|\hat{r}_2|$ oscillates in time, implying a temporal variation in the shape of the contours. Moving from the high contour levels near the centre of the core to the low contour levels near the edge of the core, the amplitude $|\hat{r}_2|$ increases and becomes more uniform in time, indicating that the outer portion of the core is more elliptic in shape and closer to steady than the inner portion. For a given contour level, $|\hat{r}_2|$ is slightly higher for the axisymmetric ring than for the planar pair. The oscillation in $|\hat{r}_2|$ seems to be approaching an asymptotic state near time $t = 75$ in the planar case and $t = 40$ in the axisymmetric case, but a transition occurs soon after; the oscillation amplitude briefly increases and the period lengthens (as we will see below, period-doubling occurs). At the final time shown in figure 11, the oscillation amplitude is returning to its pre-transition level but the period remains long.

Next we perform a spectral analysis of the oscillation in the elliptic mode. The analysis is carried out for an intermediate time interval, $15 \leqslant t \leqslant 75$ in the planar case and $10 \leqslant t \leqslant 40$ in the axisymmetric case (this avoids the initial and late-time transients). The elliptic mode is decomposed into temporal frequencies,

$$\hat{r}_2(t) = \sum_k c_k \exp(2\pi \mathrm{i} k t/L), \tag{6.2}$$

where L is the duration of the analysis ($L_{2d} = 60$, $L_{3d} = 30$). Figure 12 plots the power spectrum $|c_k|^2$ as a function of the temporal frequency k/L. At the high contour levels near the center of the core, the power spectrum has a peak frequency $f_{2d} = 46/60 = 0.77$ in the planar case and $f_{3d} = 22/30 = 0.73$ in the axisymmetric case; this is the fundamental oscillation frequency in the vortex core. For comparison, consider the passage frequency $\bar{u}/R$, defined as the inverse of the time required for the pair/ring to translate a distance equal to its radius. The passage frequency is approximately $0.1/0.8 = 0.125$ in the planar case and $0.2/0.8 = 0.25$ in the axisymmetric case. The fundamental oscillation frequency is 3–6 times greater than the passage frequency, and in this sense the core is oscillating on a moderately fast time scale.

The power spectrum in figure 12 also has a peak at the $\frac{1}{2}$-subharmonic of the fundamental in both the planar and the axisymmetric cases; this corresponds to period-doubling and is evident in the signal $|\hat{r}_2|(t)$ at late times (figure 11). In the axisymmetric case there is also a peak at the $\frac{1}{3}$-subharmonic, corresponding to period-tripling. Additional peaks can be identified in the axisymmetric case, presumably due to nonlinear interactions among the fundamental, $\frac{1}{2}$-subharmonic, and $\frac{1}{3}$-subharmonic (e.g. the frequencies $\frac{2}{3}f$ and $\frac{3}{2}f$ are evident). Moving away from the centre of the core, as the contour level is reduced, the fundamental frequency decreases slightly in amplitude and the subharmonics increase in amplitude. At the lowest contour level, the fundamental and $\frac{1}{2}$-subharmonic have equal amplitude in the planar case, while in the axisymmetric case the $\frac{1}{3}$-subharmonic is greatest. At the lowest contour level in the axisymmetric case (figure 12*h*), a peak occurs close to $\frac{1}{7}f$ but it is difficult to resolve due to the finite duration of the signal.

7. Poincaré section of the vortex sheet flow

The results obtained in § 5 and § 6 show that the vortex sheet flow undergoes a small-amplitude oscillation about a steady mean; to a good degree of approximation, the stream function of the quasi-steady flow has the form (4.2), where $\psi_0(x, y)$ represents the steady mean and $\epsilon\psi_1(x, y, t)$ is the oscillation. As discussed in § 4 in

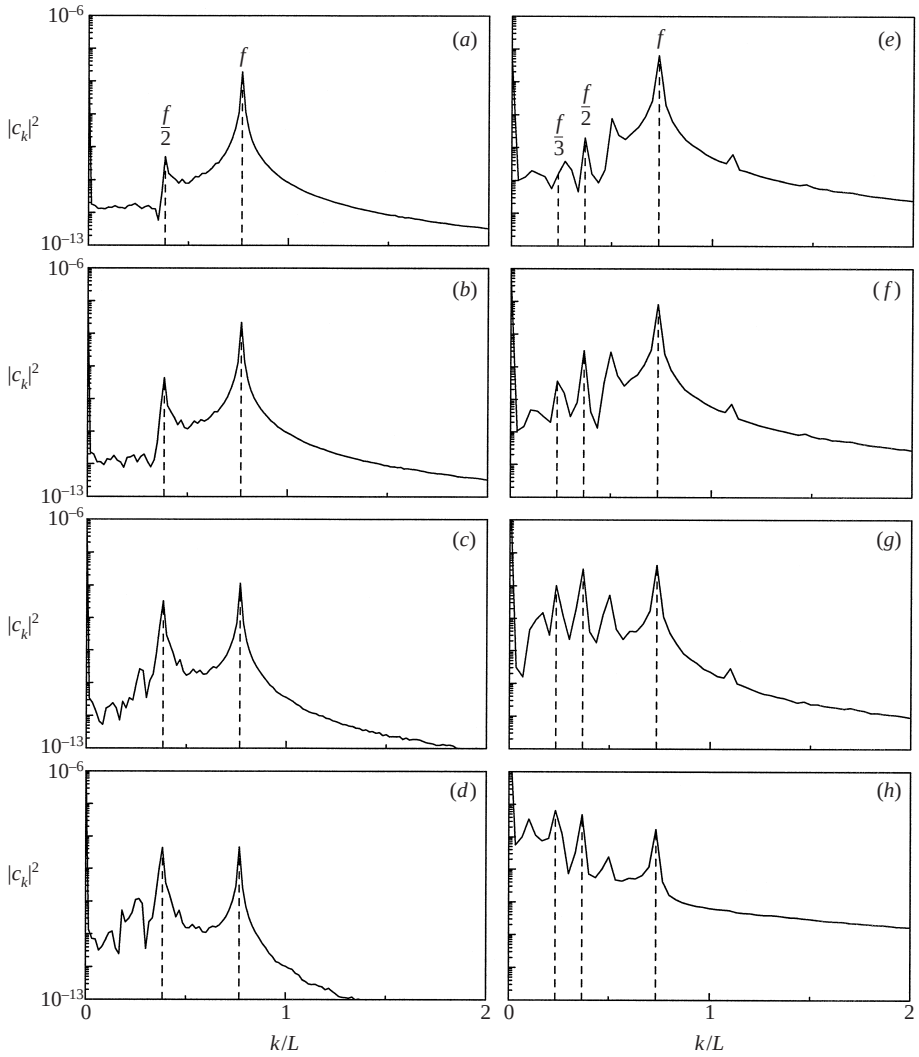

FIGURE 12. Power spectrum $|c_k|^2$ of the elliptic mode $\hat{r}_2(t)$ in the core vorticity contours (6.2), plotted as a function of temporal frequency k/L: planar (left); axisymmetric (right). The vorticity contour levels are $\omega = 3.6$ (a,e); 2.4 (b,f); 1.2 (c,g); 0.6 (d,h). Dashed lines indicate the fundamental, $\frac{1}{2}$-subharmonic, and $\frac{1}{3}$-subharmonic.

the context of the OVP model, dynamical systems theory then predicts that the corresponding Hamiltonian system (4.1) has chaotic dynamics. Rom-Kedar *et al.* (1990) used Melnikov's technique to prove that chaos occurs in the OVP model, but here we rely on numerical evidence to confirm that it also occurs in the vortex sheet flow. We do this by constructing a Poincaré section of the vortex sheet flow using the period $T = 1/f$, where $f = f_{2d}, f_{3d}$ is the fundamental oscillation frequency in the power spectrum (figure 12). Marker particles are placed throughout the flow field at time $t = 15$ and advected along with the sheet. The marker locations are recorded at multiples of the period T, up to time $t = 100$ in the planar case and $t = 60$ in the axisymmetric case.

The resulting Poincaré section is shown in figure 13. Consider first the orbits in the

vortex core. Each colour denotes a specific type of orbit: a red orbit is a resonance band, yellow orbits are periodic cycles, blue orbits are chaotic, and green orbits are either KAM curves or cantori. Each red orbit and yellow orbit has a rational rotation number p/q, indicating that the orbit returns to its initial location after p applications of the Poincaré map during which time it makes q revolutions around the core. This is strictly true only for a periodic cycle; in the case of a resonance band, the orbit does not return precisely to its initial location but merely to the island on which it was initially located. In principle, the resonance bands and periodic cycles are dense in the Poincaré section, but in practice they are difficult to locate and only a few are displayed in figure 13. Starting at the centre of the core and moving radially outward, the yellow and red orbits in the planar case have rotation numbers 2/1, 5/2, $4/1^*$, 17/2, 20/1, and in the axisymmetric case they have rotation numbers 2/1, 7/3, 3/1, 7/2, $4/1^*$, $6/1^*$, 9/1; among these, a star ($*$) denotes a resonance band and the remainder are periodic cycles. The irregular blue orbits embedded in the resonance bands are interpreted as chaotic orbits. The green orbits are interpreted as KAM curves or cantori because the markers are densely distributed on a smooth closed curve, indicating an irrational rotation number. In both the planar and axisymmetric cases, the centre of the core has only green and yellow orbits, indicating that it is a region of integrable dynamics. Surrounding this region are resonance bands with chaotic dynamics, one band in the planar case and two bands in the axisymmetric case. Further away from the centre of the core is another region of integrable dynamics, somewhat larger in the planar case than in the axisymmetric case.

The Poincaré section also displays the unstable manifold of the hyperbolic point in front of the oval. In the planar case (figure 13*a*), the manifold is represented by the orbit of a single marker (blue). The orbit is stretched near the top of the oval and compressed near the front and back, but no folding occurs; hence this is a heteroclinic orbit as in the unperturbed OVP model (figure 5*a*). In the axisymmetric case (figure 13*b*), the unstable manifold is depicted by three strands coloured red, blue, and green, respectively. The strands coincide near the front and top of the oval, but they separate and intersect transversely near the back, becoming folded and stretched in the x-direction. Each individual strand resembles an unstable manifold in a heteroclinic tangle, as in the perturbed OVP model (figure 5*b*). The presence of three strands instead of just one is attributed to the $\frac{1}{3}$-subharmonic in the power spectrum (figure 12*h*); this is explained as follows.

The unstable manifold in figure 13(*b*) was generated by placing markers along a short line segment near the front hyperbolic point at time $t = 15$. The segment was advected and recorded at multiples of the period $T = 1/f_{3d}$, but when figure 13(*b*) was plotted, the recorded segments were coloured cyclically, i.e. segments $1, 4, 7, \ldots$ were coloured red, $2, 5, 8, \ldots$ were coloured blue, and $3, 6, 9, \ldots$ were coloured green. The interpretation is that away from the centre of the core, the flow has period $3T$ rather than T, as indicated by the dominance of the $\frac{1}{3}$-subharmonic over the fundamental in the power spectrum for the lowest vorticity contour level (figure 12*h*), and the three strands depict the unstable manifold of the $3T$-periodic flow at three different phases. We note that the initial segment was chosen so that the lower endpoint is mapped into the upper endpoint after a time interval of length $3T$; this is a prerequisite for having an invariant manifold in the Poincaré section of the $3T$-periodic flow and it ensures that the collection of mapped segments for each colour forms a continuous strand.

In fact, the unstable manifold is more complicated than figure 13(*b*) suggests. By adjusting the location and length of the initial segment we could obtain a different

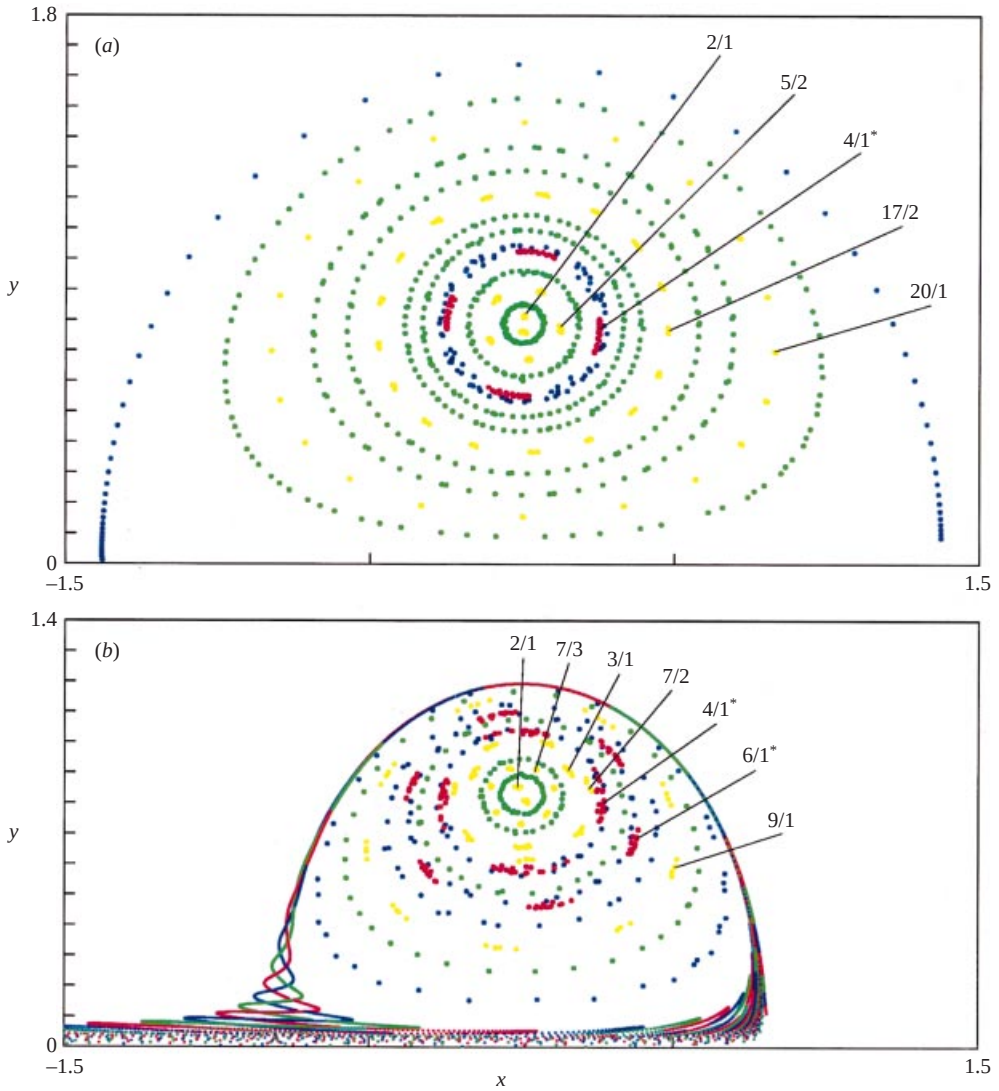

FIGURE 13. Poincaré section of the vortex sheet flow: (*a*) planar; (*b*) axisymmetric. Different types of orbits in the vortex core are colour-coded: resonance band (red), periodic cycle (yellow), chaotic orbit (blue), KAM curve or cantorus (green). The rotation number p/q is indicated for each periodic cycle and resonance band (*). The unstable manifold of the front hyperbolic point is also displayed: planar (blue), axisymmetric (red, blue, green).

number of strands; for example in one case we obtained six strands, presumably due to the fact that both the $\frac{1}{3}$- and $\frac{1}{2}$-subharmonics are present in the power spectrum (figure 12*h*). However, in these cases the strands had gaps and we were unable to adjust the initial segment to obtain continuous strands. Evidently, figure 13(*b*) represents a section of a higher-dimensional unstable manifold and the situation resembles the OVP model subject to quasi-periodic forcing (Wiggins 1992).

In summary, the Poincaré section of the vortex sheet flow displays the generic features of a chaotic Hamiltonian system: resonance bands and a heteroclinic tangle. Chaos occurs here for qualitatively the same reason as in the OVP model of Rom-

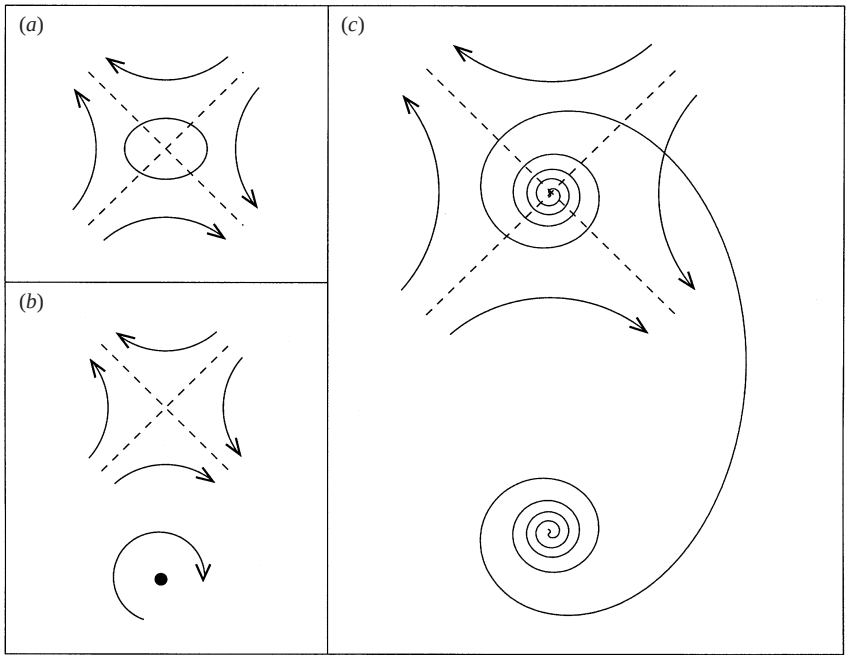

FIGURE 14. Schematic diagrams: (*a*) an elliptic vortex patch in an external strain field; (*b*) the strain induced in the far field of a point vortex; (*c*) the core of the pair/ring evolves in the strain field induced by the image core.

Kedar *et al.* (1990). Both systems have a stream function of the form (4.2); the steady mean flow has elliptic and hyperbolic points and heteroclinic orbits, and it is subject to a time-periodic perturbation (approximately so for the vortex sheet flow). Under these conditions, dynamical systems theory implies that the associated flow (4.1) is chaotic and figure 13 confirms this for the vortex sheet flow. Now since the sheet is a material curve, its shape at any instant of time reflects the history of the flow up to that time. Comparing the close-up of the sheet in figure 4 with the Poincaré section in figure 13, it is clear that the irregular features in the shape of the vortex sheet (the gaps in the spiral core and wake behind the vortex ring) are well-correlated with the resonance bands and heteroclinic tangle. Also, portions of the sheet that roll up smoothly correspond to regions of integrable dynamics in the Poincaré section. These findings lead to the conclusion that the irregular small-scale features in the shape of the vortex sheet are due to the onset of chaos in the fluid flow.

8. Discussion

8.1. *A mechanism for self-sustained oscillations*

We have seen that the vortex core undergoes a time-dependent oscillation and argued by analogy with the OVP model that this is responsible for the onset of chaos in the vortex sheet flow. However in the case of the OVP model, the oscillation is due to external forcing whereas the vortex sheet flow is not subject to such forcing. This raises a natural question: what accounts for the oscillation in the case of the vortex sheet flow?

To address this question we refer to another well-known model, an elliptic vortex patch in an external strain field. Figure 14(*a*) is a schematic diagram of the model.

Moore & Saffman (1971) showed that there exist steady states in which the self-induced rotation of the patch is balanced by the strain field. If the strain axes are aligned at 45° to the x-axis and the inclination angle is defined as the angle between the major axis of the patch and the x-axis, then a steady-state patch has zero inclination angle as depicted in figure 14(*a*). Kida (1981) found that there also exist time-dependent motions in which the patch remains elliptic in shape, but its aspect ratio and inclination angle vary in time. Among these, there are two types of time-periodic motions: one in which the inclination angle increases in time (rotation), and one in which the angle oscillates about zero (nutation). There is also a non-periodic motion in which the patch is drawn out along the axis of positive strain (elongation). It should be emphasized that these time-dependent motions of the patch occur even though the strain field is steady. For the case in which the strain field is time-periodic, Ide & Wiggins (1995) have shown that resonance bands and heteroclinic tangles can occur in the patch dynamics, and they noted as a consequence that the patch can undergo transitions between rotation, nutation, and elongation in specific regions of parameter space.

The implications for the vortex sheet flow are as follows. It is well-known that a compact region of vorticity induces strain locally in the far field (Batchelor 1967). As a simple example, consider the strain induced in the far field of a point vortex (figure 14*b*). In the case of the pair/ring in the vortex sheet flow, the vortex core above the x-axis evolves in the strain field induced by the image core below the x-axis (figure 14*c*). This effect, in the context of aircraft trailing vortices, was one of the original motivations for studying the strained vortex patch (Moore & Saffman 1971). Note that in addition to the strain induced by the image core, each vortex core also has a self-induced component of strain, so the actual situation is more complicated than suggested in figure 14(*c*). Nonetheless, it seems plausible that the total self-induced strain of the pair/ring system supports a self-sustained oscillation in the vortex core: the strain causes an elliptic deformation in the shape of the core and the deformed core undergoes an oscillation by analogy with the time-dependent motion of a strained vortex patch.

To examine this analogy, recall that the Fourier coefficient $\hat{r}_2$ describes the elliptic mode of deformation in a core vorticity contour. The oscillation in the amplitude $|\hat{r}_2|$ has already been discussed (figure 11); it corresponds to time-dependent variation in the aspect ratio of the strained vortex patch. The analogue of the patch inclination angle is the quantity $\theta_i = -\frac{1}{2}\arg\hat{r}_2$ which measures the inclination angle of the elliptic mode in a given vorticity contour. Figure 15 plots θ_i (modulo π) as a function of time for the same contour levels analysed above. The results display transitions between rotation and nutation; θ_i increases monotonically in rotation and oscillates about zero in nutation. At the highest contour level the elliptic mode initially rotates, but there is a transition to nutation near $t = 35$ in the planar case (figure 15*a*) and $t = 25$ in the axisymmetric case (figure 15*e*). A similar transition occurs earlier in time for the second highest contour level, near $t = 10$ in the planar case (figure 15*b*) and $t = 5$ in the axisymmetric case (figure 15*f*). Later in time in the planar case, near $t = 95$, there is a brief transition from nutation to rotation in the three highest contour levels. This is absent in the axisymmetric case, although the nutation amplitude increases just prior to the final simulation time. It is also evident that period-doubling occurs late in time in figure 15 (this is clearer in the planar case).

We conclude that the pair/ring system studied here supports a self-sustained oscillation in the vortex core. The core vorticity contours undergo rotation and nutation, analogous to the time-periodic motion of a vortex patch in a steady

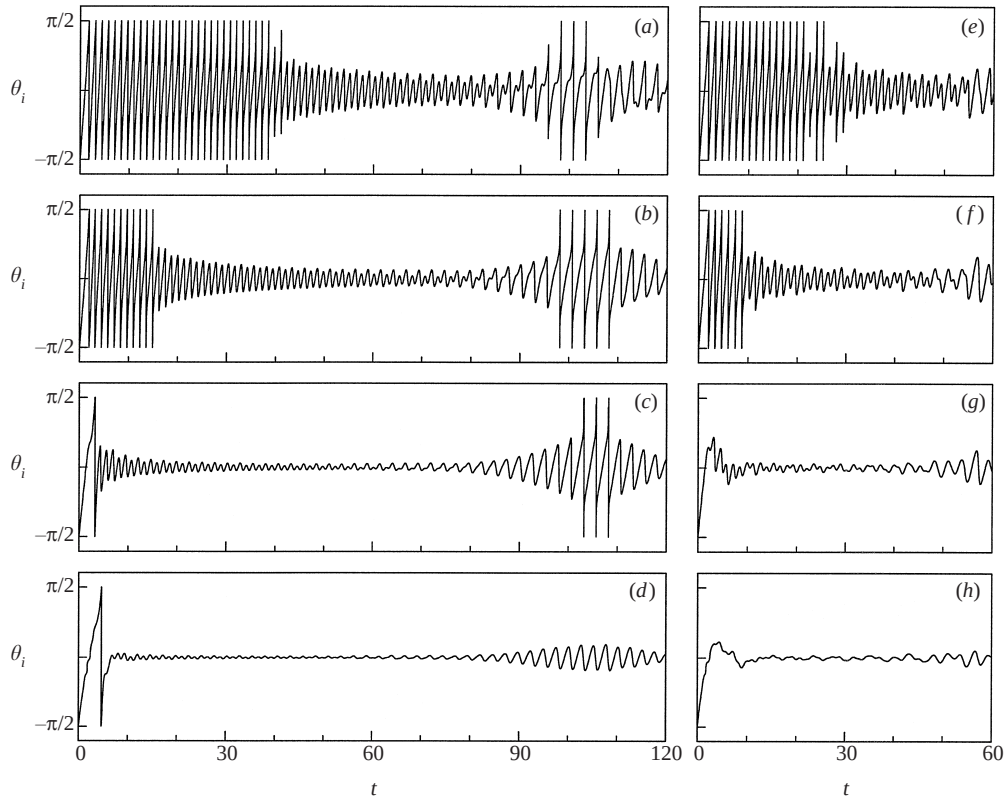

FIGURE 15. The inclination angle $\theta_i = -\frac{1}{2}\arg \hat{r}_2$ of the elliptic mode in the core vorticity contours, plotted (modulo π) as a function of time: planar (left); axisymmetric (right). The vorticity contour levels are $\omega = 3.6$ (a, e); 2.4 (b, f); 1.2 (c, g); 0.6 (d, h).

strain field (Kida 1981). We observed transitions between rotation and nutation, in qualitative agreement with the chaotic dynamics of a vortex patch in a time-periodic strain field (Ide & Wiggins 1995).

8.2. *The presence or absence of a wake*

Another question arises: why does a wake form in the axisymmetric case but not in the planar case? To address this issue we appeal again to the OVP model (Rom-Kedar *et al.* 1990). As described in § 4, given a streamline pattern as in the unperturbed OVP model (figure 5*a*), time-periodic forcing causes the stable and unstable manifolds to intersect transversely, and the unstable manifold becomes folded and stretched as $t \to +\infty$ (figure 5*b*). Material particles are ejected from the streamline oval by a turnstile mechanism and they adopt the shape of the unstable manifold. Shariff, Leonard & Ferziger (1989) and Shariff & Leonard (1992) proposed this mechanism to account for the wake seen in experiments of leap-frogging vortex rings. The vortex sheet is a material curve and it too adopts the shape of the unstable manifold (figures 4*b*, 13*b*).

Hence to explain the presence or absence of a wake, it is necessary to understand the factors responsible for transverse intersection of the stable and unstable manifolds. This is controlled by the forcing amplitude and frequency, and the corresponding parameters in the vortex sheet flow are the core oscillation amplitude and frequency.

The parameter values are comparable in the planar and axisymmetric cases (figures 11 and 12), but there is a significant difference in the geometry. In the axisymmetric case, the edge of the oval is closer to the vortex core (figures 6*f*, 7*d*, 13*b*), and so the stable and unstable manifolds are subject to higher amplitude forcing. The manifolds intersect transversely, causing a wake to form behind the vortex ring as described above. In the planar case, the edge of the oval is further away from the vortex core (figures 6*c*, 7*c*, 13*a*), and so the manifolds are subject to lower amplitude forcing. The manifolds fail to intersect transversely and no wake forms behind the vortex pair (figures 4*a*, 13*a*).

9. Summary and concluding remarks

We have presented regularized point-vortex simulations of vortex sheet motion in planar and axisymmetric flow. The sheet forms a vortex pair in the planar case and a vortex ring in the axisymmetric case. Initially the sheet rolls up into a smooth spiral, but irregular small-scale features develop later in time: gaps and folds appear in the spiral core and a wake is shed behind the vortex ring. These features are due to the onset of chaos in the vortex sheet flow. We justified this conclusion by drawing an analogy with the oscillating vortex pair (OVP) model of Rom-Kedar *et al.* (1990).

The vortex sheet flow has much in common with the OVP model. They both have stream functions of the form (4.2), a steady mean flow with a small-amplitude time-dependent perturbation. The mean flows have the same pattern of elliptic and hyperbolic points and heteroclinic orbits. The perturbations are similar as well, time-periodic for the OVP model and approximately so for the vortex sheet flow. Under these conditions, general results from dynamical systems theory imply that the associated flow (4.1) is chaotic. To verify this for the vortex sheet flow, we constructed a Poincaré section and observed that it has the generic features of a chaotic Hamiltonian system: resonance bands and a heteroclinic tangle. These features in the Poincaré section are well-correlated with the irregular features in the shape of the vortex sheet. The Poincaré section also has KAM curves bounding regions of integrable dynamics in which the sheet rolls up smoothly.

The two models also have some significant differences. The OVP model is subject to external forcing while the vortex sheet flow has a self-sustained oscillation in the vortex core. The core vorticity contours are almost circular, but there is a slight elliptic deformation that oscillates in a manner resembling the motion of a strained vortex patch (Kida 1981). In the case of the OVP model, there is chaotic advection of passive particles in the induced velocity field, but the vorticity distribution has integrable dynamics. In the case of the vortex sheet flow, transitions occur between rotation and nutation suggesting that the vorticity distribution itself has chaotic dynamics, as for a vortex patch in a time-periodic strain field (Ide & Wiggins 1995).

Even if one accepts the idea that the vortex core has a self-sustained oscillation, a number of other questions remain. Spectral analysis of the oscillation showed that the fundamental frequency is almost the same in the planar and axisymmetric cases. The $\frac{1}{2}$-subharmonic is present in both cases and the $\frac{1}{3}$-subharmonic occurs in the axisymmetric case. The detailed selection mechanism for these frequencies is unclear.

The simulations used a representative value for the smoothing parameter ($\delta = 0.2$). Previous work showed that reducing δ causes the sheet to roll up faster and more tightly, and the evidence suggested that the regularized solutions converge to a smooth well-defined spiral in the limit $\delta \to 0$ (Krasny 1987). However, the present results show that the situation is more complex and the limiting behaviour for $\delta \to 0$ is unclear. In

particular it is not known to what extent chaos persists in the limit $\delta \to 0$. Similarly, there are not yet any data showing the effect of δ on the oscillation amplitude and frequency. Another interesting question is the long-time behaviour for a fixed value of δ. Progress on these issues will probably require using multiple precision arithmetic, parallel computing, and fast treecode algorithms (Draghicescu & Draghicescu 1995; Lindsay & Krasny 2001).

The present work is concerned with idealized planar and axisymmetric flows, and one can question whether the results are relevant to real flows. In fact, there are some hints of the present findings in the experimental literature. Glezer (1988, figure 1*a*) displayed an experimental flow visualization of a vortex ring oval with a long thin folded wake that resembles the present figure 2(*b*) at the final simulation time. Zaitsev *et al.* (1990) measured the sound emitted by a translating vortex ring and found that the acoustic spectrum has a peak frequency. To account for the observed spectrum, Shariff & Leonard (1992) proposed the elliptic core model of Moore (1980), while Zaitsev & Kop'ev (1993) proposed an elliptic Kelvin mode on the edge of the core. These findings suggest that the core oscillation and chaotic dynamics seen here might possibly occur in real flows, but further study is needed in order to make a definite conclusion.

We thank Christopher K. R. T. Jones, Vered Rom-Kedar and Karim Shariff for valuable discussions. This work was supported by NSF grants DMS-9506452, DMS-9973293 and DMS-9996254.

REFERENCES

Anderson, C. R. 1985 A vortex method for flows with slight density variations. *J. Comput. Phys.* **61**, 417–444.

Aref, H. 1983 Integrable, chaotic and turbulent vortex motion in two-dimensional flows. *Annu. Rev. Fluid Mech.* **15**, 345–389.

Aref, H. 1984 Stirring by chaotic advection. *J. Fluid Mech.* **143**, 1–21.

Batchelor, G. K. 1967 *An Introduction to Fluid Dynamics*. Cambridge University Press.

Bertozzi, A. L. 1988 Heteroclinic orbits and chaotic dynamics in planar fluid flows. *SIAM J. Math. Anal.* **19**, 1271–1294.

Birkhoff, G. 1961 Helmholtz and Taylor instability. *Proc. Symp. Appl. Math.* **XIII**, 55–76.

Brady, M., Leonard, A. & Pullin, D. I. 1998 Regularized vortex sheet evolution in three dimensions. *J. Comput. Phys.* **146**, 520–545.

Caflisch, R., Li, X. & Shelley, M. 1993 The collapse of an axi-symmetric, swirling vortex sheet. *Nonlinearity* **6**, 843–867.

Chorin, A. J. & Bernard, P. S. 1973 Discretization of a vortex sheet, with an example of roll-up. *J. Comput. Phys.* **13**, 423–429.

Couder, Y. & Basdevant, C. 1986 Experimental and numerical study of vortex couples in two-dimensional flows. *J. Fluid Mech.* **173**, 225–251.

Dahm, W. J. A., Frieler, C. E. & Tryggvason, G. 1992 Vortex structure and dynamics in the near field of a coaxial jet. *J. Fluid Mech.* **241**, 371–402.

Dhanak, M. R. & Marshall, M. P. 1993 Motion of an elliptical vortex under applied periodic strain. *Phys. Fluids* A **5**, 1224–1230.

Draghicescu, C. & Draghicescu, M. 1995 A fast algorithm for vortex blob interactions. *J. Comput. Phys.* **116**, 69–78.

Glezer, A. 1988 The formation of vortex rings. *Phys. Fluids* **31**, 3532–3542.

Guckenheimer, J. & Holmes, P. 1983 *Nonlinear Oscillations, Dynamical Systems and Bifurcations of Vector Fields*. Springer.

Ide, K. & Wiggins, S. 1995 The dynamics of elliptically shaped regions of uniform vorticity in time-periodic, linear external velocity fields. *Fluid Dyn. Res.* **15**, 205–235.

Kida, S. 1981 Motion of an elliptic vortex in a uniform shear flow. *J. Phys. Soc. Japan* **50**, 3517–3520.

Krasny, R. 1986 A study of singularity formation in a vortex sheet by the point-vortex approximation. *J. Fluid Mech.* **167**, 65–93.

Krasny, R. 1987 Computation of vortex sheet roll-up in the Trefftz plane. *J. Fluid Mech.* **184**, 123–155.

Lamb, H. 1932 *Hydrodynamics*. Dover.

Lim, T. T. & Nickels, T. B. 1995 Vortex rings. In *Fluid Vortices* (ed. S. I. Green), pp. 95–153. Kluwer.

Lindsay, K. & Krasny, R. 2001 A particle method and adaptive treecode for vortex sheet motion in three-dimensional flow. *J. Comput. Phys.* **172**, 879–907.

Lopez, J. M. & Perry, A. D. 1992 Axisymmetric vortex breakdown. Part 3. Onset of periodic flow and chaotic advection. *J. Fluid Mech.* **234**, 449–471.

Miller, P. D., Jones, C. K. R. T., Rogerson, A. M. & Pratt, L. J. 1997 Quantifying transport in numerically generated velocity fields. *Physica* D **110**, 105–122.

Montgomery, D., Matthaeus, W. H., Stribling, W. T., Martinez, D. & Oughton, S. 1992 Relaxation in two dimensions and the "sinh-Poisson" equation. *Phys. Fluids* A **4**, 3–6.

Moore, D. W. 1979 The spontaneous appearance of a singularity in the shape of an evolving vortex sheet. *Proc. R. Soc. Lond.* A **365**, 105–119.

Moore, D. W. 1980 The velocity of a vortex ring with a thin core of elliptical cross-section. *Proc. R. Soc. Lond.* A **370**, 407–415.

Moore, D. W. & Saffman, P. G. 1971 Structure of a line vortex in an imposed strain. In *Aircraft Wake Turbulence and its Detection* (ed. J. H. Olsen, A. Goldburg & M. Rogers), pp. 339–354. Plenum.

Neu, J. 1984 The dynamics of a columnar vortex in an imposed strain. *Phys. Fluids* **27**, 2397–2402.

Newton, P. K. 2001 *The N-Vortex Problem*. Springer.

Nitsche, M. 1998 Core dynamics in vortex pairs and rings. In *Proc. IUTAM Symp. on Dynamics of Slender Vortices* (ed. E. Krause & K. Gersten), pp. 143–152. Kluwer.

Nitsche, M. & Krasny, R. 1994 A numerical study of vortex ring formation at the edge of a circular tube. *J. Fluid Mech.* **276**, 139–161.

Ottino, J. M. 1989 *The Kinematics of Mixing: Stretching, Chaos, and Transport*. Cambridge University Press.

Polvani, L. M. & Wisdom, J. 1990 Chaotic Lagrangian trajectories around an elliptical vortex patch embedded in a constant and uniform background shear flow. *Phys. Fluids* A **2**, 123–126.

Pozrikidis, C. 2000 Theoretical and computational aspects of the self-induced motion of three-dimensional vortex sheets. *J. Fluid Mech.* **425**, 335–366.

Pullin, D. I. 1978 The large-scale structure of unsteady self-similar rolled-up vortex sheets. *J. Fluid Mech.* **88**, 401–430.

Rom-Kedar, V., Leonard, A. & Wiggins, S. 1990 An analytical study of transport, mixing and chaos in an unsteady vortical flow. *J. Fluid Mech.* **214**, 347–394.

Saffman, P. G. 1992 *Vortex Dynamics*. Cambridge University Press.

Sakajo, T. 2001 Numerical computation of a three-dimensional vortex sheet in a swirl flow. *Fluid Dyn. Res.* **28**, 423–448.

Shariff, K. & Leonard, A. 1992 Vortex rings. *Annu. Rev. Fluid Mech.* **24**, 235–279.

Shariff, K., Leonard, A. & Ferziger, J. H. 1989 Dynamics of a class of vortex rings. *NASA TM*-102257.

Shariff, K., Verzicco, R. & Orlandi, P. 1994 A numerical study of three-dimensional vortex ring instabilities: viscous corrections and early nonlinear stage. *J. Fluid Mech.* **279**, 351–375.

Spalart, P. R. 1998 Airplane trailing vortices. *Annu. Rev. Fluid Mech.* **30**, 107–138.

Stevens, J. L., Lopez, J. M. & Cantwell, B. J. 1999 Oscillatory flow states in an enclosed cylinder with a rotating endwall. *J. Fluid Mech.* **389**, 101–118.

Wiggins, S. 1992 *Chaotic Transport in Dynamical Systems*. Springer.

Ye, Q.-Y. & Chu, C. K. 1995 Unsteady evolutions of vortex rings. 1995 *Phys. Fluids* **7**, 795–801.

Zaitsev, M. Yu. & Kop'ev, V. F. 1993 Mechanism of sound radiation by a turbulent vortex ring. *Acoust. Phys.* **39**, 562–565.

Zaitsev, M. Yu., Kop'ev, V. F., Munin, A. G. & Potokin, A. A. 1990 Sound radiation by a turbulent vortex ring. *Sov. Phys. Dokl.* **35**, 488–489.